nature geoscience

Article

https://doi.org/10.1038/s41561-022-01089-9

Mineral-catalysed formation of marine NO and N_2O on the anoxic early Earth

Received: 30 January 2021

Accepted: 18 October 2022

Published online: 5 December 2022

Check for updates

Steffen Buessecker[1,9] ✉, Hiroshi Imanaka[2,3], Tucker Ely[4], Renyu Hu[5,6], Stephen J. Romaniello[4,7] & Hinsby Cadillo-Quiroz[1,8]

Microbial denitrification converts fixed nitrogen species into gases in extant oceans. However, it is unclear how such transformations occurred within the early nitrogen cycle of the Archaean. Here we demonstrate under simulated Archaean conditions mineral-catalysed reduction of nitrite via green rust and magnetite to reach enzymatic conversion rates. We find that in an Fe^{2+}-rich marine environment, Fe minerals could have mediated the formation of nitric oxide (NO) and nitrous oxide (N_2O). Nitrate did not exhibit reactivity in the presence of either mineral or aqueous Fe^{2+}; however, both minerals induced rapid nitrite reduction to NO and N_2O. While N_2O escaped into the gas phase (63% of nitrite nitrogen, with green rust as the catalyst), NO remained associated with precipitates (7%), serving as a potential shuttle to the benthic ocean. Diffusion and photochemical modelling suggest that marine N_2O emissions would have sustained 0.8–6.0 parts per billion of atmospheric N_2O without a protective ozone layer. Our findings imply a globally distributed abiotic denitrification process that feasibly aided early microbial life to accrue new capabilities, such as respiratory metabolisms.

Before the rise of O_2 during the Great Oxidation Event (GOE), the Archaean ocean received oxides of nitrogen (NO_x) by deposition of abiotic nitrogen fixation products[1]. As a consequence, nitrite (NO_2^-) and nitrate (NO_3^-) reached seawater concentrations in the lower micrometre range[1–4]. While microbial denitrification plays a dominant role in modern oceans in recycling NO_x^- into gaseous phases, such pathways were not available in the Archaean without active NO_x^- reductases. A non-enzymatic process reducing fixed NO_x^- into gases is chemodenitrification, which is of particular interest because nitrous oxide (N_2O) can be a primary product[5–7]. The Archaean atmosphere before the GOE was probably dominated by N_2 and CO_2, with ppm levels of CO, CH_4 and H_2 (ref. [8]). The introduction of even trace amounts of more oxidized gases, such as N_2O, could have created a critical source of thermodynamic disequilibrium to drive primitive ecosystems. Furthermore, N_2O is a strong greenhouse gas and has been considered to induce a warmer climate under a faint young Sun[9]. Stanton et al.[10] first showed through experiments and modelling that aqueous Fe^{2+} could have acted as a driver for chemodenitrification to form N_2O abiotically in Proterozoic oceans. Yet, N_2O production rates established for the early marine environment, thus far, have been around four orders of magnitude lower than rates reported from isotope tracer measurements in modern oxygen minimum zones (Table 1), underlining the catalytic importance of denitrification enzymes for rapid nitrogen cycling. As a result, it has been hypothesized that N_2O was virtually absent on the anoxic early Earth, especially without a protective ozone (O_3) layer to compensate for elevated photolytic N_2O destruction[11–13]. While under ferruginous conditions aqueous Fe^{2+} has not stimulated N_2O production close to microbially mediated rates (Table 1), mineral phases bear the potential to reach such rates and could have therefore provided efficient pathways to channel fixed nitrogen back into the Archaean atmosphere.

[1]School of Life Sciences, Arizona State University, Tempe, AZ, USA. [2]SETI Institute, Mountain View, CA, USA. [3]NASA Ames Research Center, Mountain View, CA, USA. [4]School of Earth and Space Exploration, Arizona State University, Tempe, AZ, USA. [5]Jet Propulsion Laboratory, California Institute of Technology, Pasadena, CA, USA. [6]Division of Geological and Planetary Sciences, California Institute of Technology, Pasadena, CA, USA. [7]Department of Earth and Planetary Sciences, University of Tennessee, Knoxville, TN, USA. [8]Biodesign Institute, Arizona State University, Tempe, AZ, USA. [9]Present address: Department of Earth System Science, Stanford University, Stanford, CA, USA. ✉e-mail: sbuessecker@stanford.edu

https://doi.org/10.1038/s41561-022-01089-9

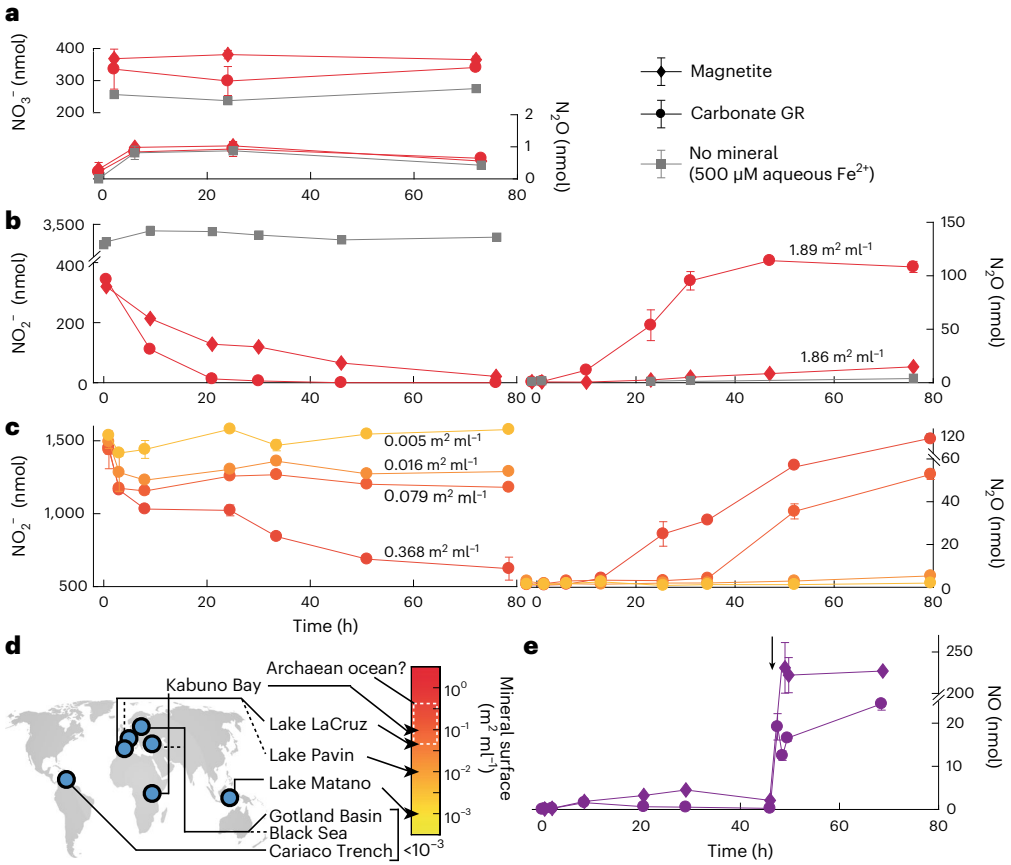

Fig. 1 | Molecular NO_x^- consumption and associated NO and N_2O production with Fe minerals or aqueous Fe^{2+}. **a**–**e**, Dissolved NO_3^- and NO_2^- in anoxic artificial seawater solution were quantified concomitantly to NO and N_2O in the headspace. The results from incubations with initial NO_x^- concentrations in the high (20–35 µM) range are shown (all incubation results are provided in Supplementary Table 1). The *y* axes depict total quantities (gas + liquid phase) and are sometimes interrupted by breaks to better illustrate changes. **a**, NO_3^- amended microcosms with green rust and magnetite. **b**, NO_2^- amended microcosms with green rust and magnetite. **c**, NO_2^- reduction and N_2O production under varying green rust concentrations. After initial rapid NO_2^- consumption, the reaction may become mineral surface limited, hindering the reduction of more NO_2^-. **d**, The range of green rust surface area was informed by naturally occurring Fe mineral particles in modern Archaean ocean analogues (Supplementary Information). **e**, NO formation with 33 µM initial NO_2^- and a mineral concentration identical to **b**. The arrow indicates the addition of concentrated hydrochloric acid, resulting in subsequent mineral particle dissolution and outgassing of NO. The data are presented as mean values ± s.d. ($n = 3$).

Here we evaluated the role of the mineral-catalysed formation of NO and N_2O as a marine source pathway under anoxic, ferruginous conditions. NO has been measured in mixtures of NO_x^- and highly concentrated Fe^{2+} solutions[5], and in an MoS_2 suspension under a geoelectric current[14], but it has only been speculated to be produced in Fe mineral suspensions[6,7]. The ferrous–ferric hydroxy salt carbonate green rust (GR; $[Fe^{2+}_{(1-x)}\,Fe^{3+}_{x}\,(OH)_2]^{x+} \cdot [(x/2)CO_3^{2-} \cdot (m/2)H_2O]^{x-}$) has been shown to precipitate from Archaean seawater–analogue solutions, consistent with thermodynamics predicting a predominance of GR in the Fe sink fraction along the water column before 2.5–2.7 Ga[15]. Settling GR particles could have provided a transport mechanism for trace compounds to the seafloor[15], where reducing conditions partially converted GR to magnetite (Fe_3O_4), an important constituent of banded iron formations. Because NO_2^- and NO_3^- can react spontaneously in the presence of reduced Fe[16–18], we tested the reactivity of the mixed-valence Fe minerals GR and magnetite with NO_2^- and NO_3^- at low (1–5 µM), high (20–35 µM) and excessive (200–350 µM) abundances, and characterized their potential to produce NO and N_2O at relevant rates for the Archaean ocean–atmosphere system. To do so, we used mineral particle concentrations recorded for modern analogues as a proxy for mineral abundance (Supplementary Figs. 1–4). We experimentally simulated ferruginous conditions with a simple end-member artificial seawater recipe using a 20% CO_2–HCO_3^- buffer devoid of sulfur. Subsequent flux and photochemical calculations suggested that mineral-catalysed NO and N_2O formation constituted a substantial marine source of gaseous nitrogen oxides on the anoxic early Earth.

Abiotic NO_x^- reduction under simulated Archaean conditions

First, we compared the reactivity of NO_3^- and NO_2^- with GR, magnetite and aqueous Fe^{2+} separately. For all reductants, the consumption of NO_3^- and production of N_2O was negligible (<0.03 nmol h^{-1}; Fig. 1a), even over a prolonged period of 100 d. In contrast, NO_2^- showed reactivity in the presence of both mineral catalysts and was stable in controls with 500 µM aqueous Fe^{2+}. The contrasting reactivity of the nitrogen oxides is reflected in the solid-phase Fe^{2+}/Fe^{3+} ratio determined at the end of the experiment (Fig. 2), revealing a trend of higher mineral oxidation with increasing NO_2^- concentration. Magnetite and GR showed disparate potential to produce N_2O. Concomitant with a more rapid NO_2^- consumption, N_2O production rates were more than ten times higher when GR was the catalyst (Fig. 1b). At GR surface areas observed for the Archaean ocean analogue Lake Matano, Indonesia[19] (~10^{-3} m^2 ml^{-1}; Fig. 1c,d), abiotic N_2O production rates were highly similar to (low NO_2^-) or exceeding (high NO_2^-) biotic production rates measured recently in the Eastern Tropical North Pacific[20,21] (Table 1). As a reference, modern NO_2^- concentrations are near the bottom of the experimental range

https://doi.org/10.1038/s41561-022-01089-9

Table 1 | N_2O and NO production rates of the modern and early marine environment and from cultured microbial species

Earth period	System	N_2O/NO production rate (nM d^{-1})	Reference(s)
N_2O			
Modern	Eastern Tropical North Pacific	0.5–5.0	Refs. [20,21]
Modern	Arabian Sea	0.005–0.080	Ref. [59]
Modern	Eastern Tropical South Pacific	6.0–43.2	Ref. [60]
Modern	Eastern Tropical North Atlantic	1.5–3.5	Ref. [61]
Modern	Peruvian coastal upwelling zone	5–49	Ref. [62]
Modern	Cultured *Nitrosomonas marina* C-113a	2–3	Ref. [63]
Modern	Cultured *Nitrosomonas marina* NM22	1.4–4.2	Ref. [61]
Modern	Cultured *Nitrosococcus oceani* NC10	1.2–3.7	Ref. [61]
Modern	Cultured *Nitrosopumilus maritimus* SCM1	0.4–24.3	Ref. [61]
Early	Simulated ferruginous ocean with aqueous Fe^{2+}	0.0001–0.0100	Ref. [10]
Early	Simulated ferruginous ocean with GR particles	0.3–17.9[a]	This study
NO			
Modern	Equatorial Pacific, near 170° West	34.6–103.7	Ref. [64]
Modern	Yellow Sea	129.6	Ref. [65]
Modern	Cultured *Nitrosopumilus maritimus* SCM1	4,800	Ref. [66]
Early	Simulated ferruginous ocean with GR particles	≥737.5[b]	This study

[a]Derived from incubations with low NO_2^- abundances and 0.005–0.366 m^2 ml^{-1} GR surface.
[b]Estimate of total (free and mineral-associated) NO based on particle dissolution after 50 h in incubations with high NO_2^- abundances.

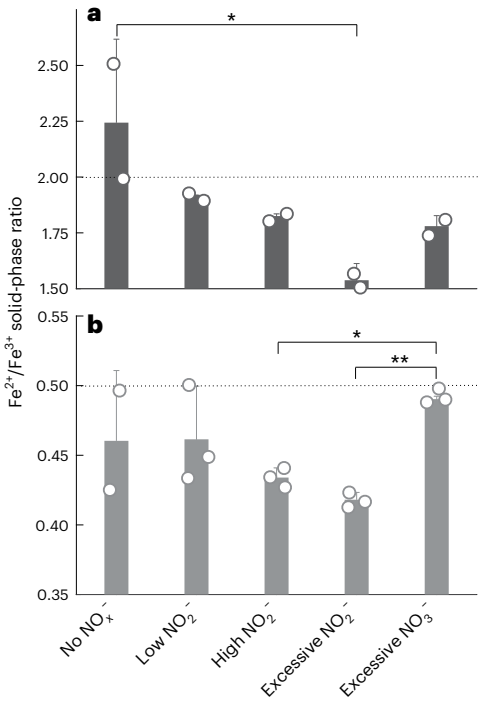

Fig. 2 | Solid-phase ratios of reduced and oxidized Fe in green rust and magnetite. a,**b**, Solid-phase ratios of reduced and oxidized Fe in green rust (**a**) and magnetite (**b**). The data were collected after acid digestion at the end of incubations. The dotted lines indicate stoichiometric green rust and magnetite, respectively. For total Fe abundances, see Supplementary Table 2. *P = 0.02 and **P = 0.006 (two-sided Student's t-test). The columns indicate mean values and error bars denote one s.d. based on n = 2 (**a**) and n = 3 (**b**).

employed here, which extends higher to account for a range of possible Archaean NO_x^- abundances (see discussion below).

The conversion of NO_2^- to N_2O was not equimolarily balanced and we therefore considered the accumulation of NO as intermediary species[7]. After initially observing modest NO accumulation, we injected concentrated hydrochloric acid to dissolve mineral particles and release any nitrogen bound to mineral surfaces. Indeed, the particle dissolution was followed by a spike in headspace NO (Fig. 1e). At least 92% of the total NO was bound to GR (97% was bound to magnetite). To rule out reaction of the acid with residual NO_2^-, we conducted controls with sulfuric acid and NO_2^- (Supplementary Table 3). Other controls evaluating the stability of NO in the mineral suspension included acid injection at later time points in time-extended experiments. NO yields at 220 h (<0.5 µM NO_2^-) were similar to those at 50 h after NO_2^- addition (Supplementary Fig. 5 and Supplementary Table 3). We calculated the NO yield in respect to total NO_2^- and, accordingly, 7% reacted to NO (compared to 63% that reacted to N_2O) with GR as the catalyst and 87% reacted to NO (compared to 8% that reacted to N_2O) with magnetite as catalyst. The remaining product pool could be N_2 (ref. [7]) and only constituted a minor fraction. Our data show that mineral-associated NO—presumably in the form of nitrosyl species[22]—is an important byproduct and geochemically stable in the presence of Fe mineral phases.

N_2O accumulation triggered by marine emissions

To elucidate the impact of the experimentally derived production rates on N_2O dispersion in seawater and emissions to the Archaean atmosphere, we combined diffusion models into a simple flux balance model (Supplementary Information). We considered a 100 m deep ocean slab beneath the photic zone as the part of the water column with maximum overlap of NO_x^- ions from the surface and GR formation fuelled by upwelling Fe^{2+}-rich water from the depths. An estimate of the GR particle concentration in the Archaean ocean was informed by observed Fe particle numbers from seven modern marine and freshwater anoxic basins (Fig. 1d), including Kabuno Bay, East Africa[23]. The peak Fe^{2+} concentration in the particulate fraction of Kabuno Bay waters (11 µM) closely reflects concentrations used for the thermodynamic modelling of GR precipitation in Archaean seawater[15], which is why we used the Kabuno Bay level as a reference and enveloped that value with putative lower and upper boundaries of 50% and 500%. Archaean seawater Fe^{2+} could have reached concentrations of 55 µM, as constrained by Fe^{2+} toxicities on cyanobacteria[24] and the appearance of herringbone and micritic carbonates[25,26]. At that upper boundary and under low (conservative) NO_2^- conditions, net N_2O emissions conceivably reached 235 nmol m^{-2} h^{-1} (95% confidence interval = 98.1–413.9 m^{-2} h^{-1}; Supplementary Figs. 6 and 7 and Supplementary Table 4), implicating four times the modern marine average flux[27]. Overall, N_2O emissions from the ferruginous ocean gradually increased with GR particle concentration.

To simulate the effect of N_2O fluxes triggered by mineral catalysis into an anoxic Archaean atmosphere, we applied a photochemical model[28]. We probed four different N_2O fluxes corresponding to low and high NO_2^- levels and Fe^{2+} concentrations in GR phases around the Kabuno Bay reference (Supplementary Table 4). Although the upper boundary of our estimates implicates near-modern N_2O abundances in

https://doi.org/10.1038/s41561-022-01089-9

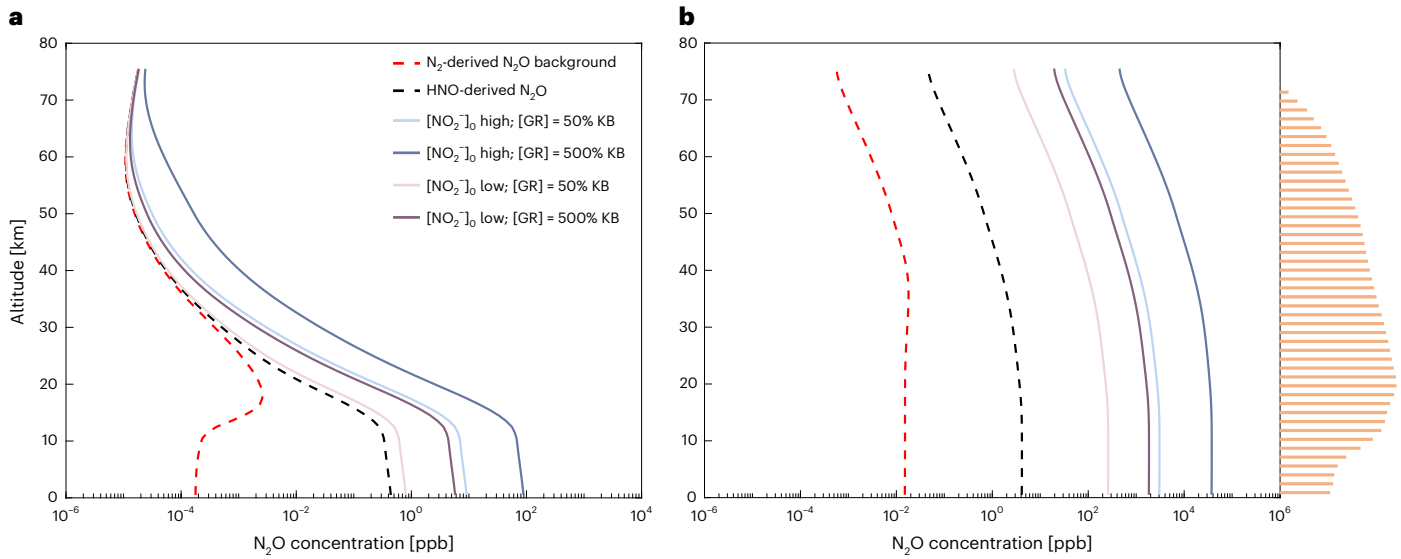

Fig. 3 | Atmospheric N_2O under the influence of mineral-catalysed N_2O production in the Archaean ocean. a, Atmospheric N_2O abundance by altitude, based on fluxes assuming green rust phases in Kabuno Bay (KB) equivalents with low and high seawater NO_2^- levels. Background N_2O formation occurred via the reaction $N_2 + O(^1D) + M \rightarrow N_2O + M$, and $O(^1D)$ was produced by photodissociation of CO_2 with photons more energetic than 167 nm. N_2O can also be derived directly through dehydrative dimerization of HNO that did not polymerize into NO_3^- or NO_2^- (ref. [34]). N_2O profiles do not account for N_2O from the HNO pathway. **b**, Atmospheric N_2O abundances when a fractal haze layer is included in the photochemical model. We adopt the fractal haze predicted by ref. [31] for the Archaean atmosphere, which has an optical depth of ~10 at 200 nm and only ~0.6 at 500 nm. The bars to the right illustrate the relative haze absorption based on data from ref. [31]. N_2O builds up to much higher abundances because of the strong shielding effect of the haze.

the troposphere (0–13 km altitude; Fig 3), N_2O concentrations derived from low NO_2^- seawater levels, and predicted to be 0.8–6.0 parts per billion (ppb), are more realistic. These concentrations match mixing ratios in previous Proterozoic atmosphere models assuming 1% of present O_2 levels[10,13]. However, a striking difference is the inclusion of an O_3 protective layer in previous models, which was assumed to be present after the GOE, that is in the Proterozoic. Our photochemical model produced an ozone column of ~9.6×10^{14} molecules per cm, which is less than the present-day level by four orders of magnitude and less than previously modelled Proterozoic levels by around three orders of magnitude. Thus, without the aid of O_3 shielding, marine mineral-catalysed N_2O production generated tropospheric N_2O levels akin to those in oxygenated atmospheres later in Earth's history.

The main sink of N_2O is photolysis by radiation at <230 nm[29] in the stratosphere, which governs the shape of the concentration profiles (Fig. 3a). In the Archaean atmosphere, N_2O abundances could have been higher due to: (1) additional sources; and (2) protective agents against ultraviolet light. For instance, high-energy particles from solar flares led to N_2O formation that was most active at higher altitudes and could complement surface sources[30]. These pathways were perhaps more pronounced in the Hadean or early Archaean when the Sun was more active and the magnetic field openings were greater at the poles. Furthermore, in the presence of methane hazes, N_2O could have been shielded through strong ultraviolet absorption by fractal haze particles[31], which prolonged its lifetime. A sensitivity study using the photochemical model shows that, with a fractal haze, N_2O concentrations derived from low NO_2^- seawater levels can build up to one to seven times the present-day atmospheric level (Fig. 3b). One may ask whether this buildup of abiotic N_2O may constitute a false positive scenario for using N_2O as a biosignature gas for terrestrial exoplanets akin to the Archaean Earth. We suggest that this would not be a true false positive because the high abundance of methane, which is the prerequisite of the fractal haze layer, is probably biogenic in the first place.

Despite the extent of tropospheric N_2O predicted by our model, effects on the planetary climate were probably modest because N_2O would not be sufficiently concentrated to markedly increase the infrared atmospheric opacity in CO_2 window regions. Especially under high CO_2 atmospheres, the N_2O radiative forcing is diminished since it may not occupy otherwise transparent infrared windows. The infrared window between 6 and 8 μm could potentially be filled by N_2O absorption, but this is dependent on atmospheric methane, which absorbs at similar wavelengths[13]. Since methane concentrations were probably >100 parts per million by volume[32], greenhouse warming by N_2O under our simulated conditions therefore contributed only weakly to a warmer climate under the faint young Sun of the Archaean[9].

Fe mineral reactions as a potent sink for marine NO_x^-

Because of prevailing ferruginous conditions, mineral reactions were probably limited by abiotic nitrogen fixation rates rather than mineral surface area. Previous seawater NO_x^- estimations (8.7–24,000 μM[2], 1–10,000 μM[33], <1 μM[4] and 0.2–2 μM[34]) contain a large uncertainty. For comparison, modern NO_2^- concentrations reach ~1.5 μM around oxygen minimum zones, but in contrast with the Archaean ocean, oxidoreductases effectively suppress NO_2^- accumulation[35]. While previous estimates refer to the average bulk seawater composition, top-down gradients of NO_x^- or conical zones of higher NO_x^- concentrations beneath rainout areas contributed perhaps to a more heterogeneous distribution. In such zones, NO_x^- may have reached steady-state concentrations well above the low NO_x^- range (1–5 μM) designated here.

Our experimental data suggest rapid consumption of seawater NO_x^- (NO_2^- in particular), revealing a sink distributed over the pelagic ocean that has thus far not been accounted for. Previously proposed geochemical reactions that consumed dissolved NO_x^- species on the early Earth included reduction to ammonia[36] and reduction of NO_3^-, NO_2^- and N_2 during water–rock interactions between hydrothermal fluids and the oceanic crust[33,37,38]. However, abiotic NO_x^- conversion to ammonia is not significant at pH ≤ 7.3 (ref. [36])—a regimen that dominated the early oceans[39] and therefore restricted this NO_x^- sink to more alkaline environments, such as ultramafic-hosted hydrothermal vents. Because NO_3^- was photo-reduced to NO_2^- and

https://doi.org/10.1038/s41561-022-01089-9

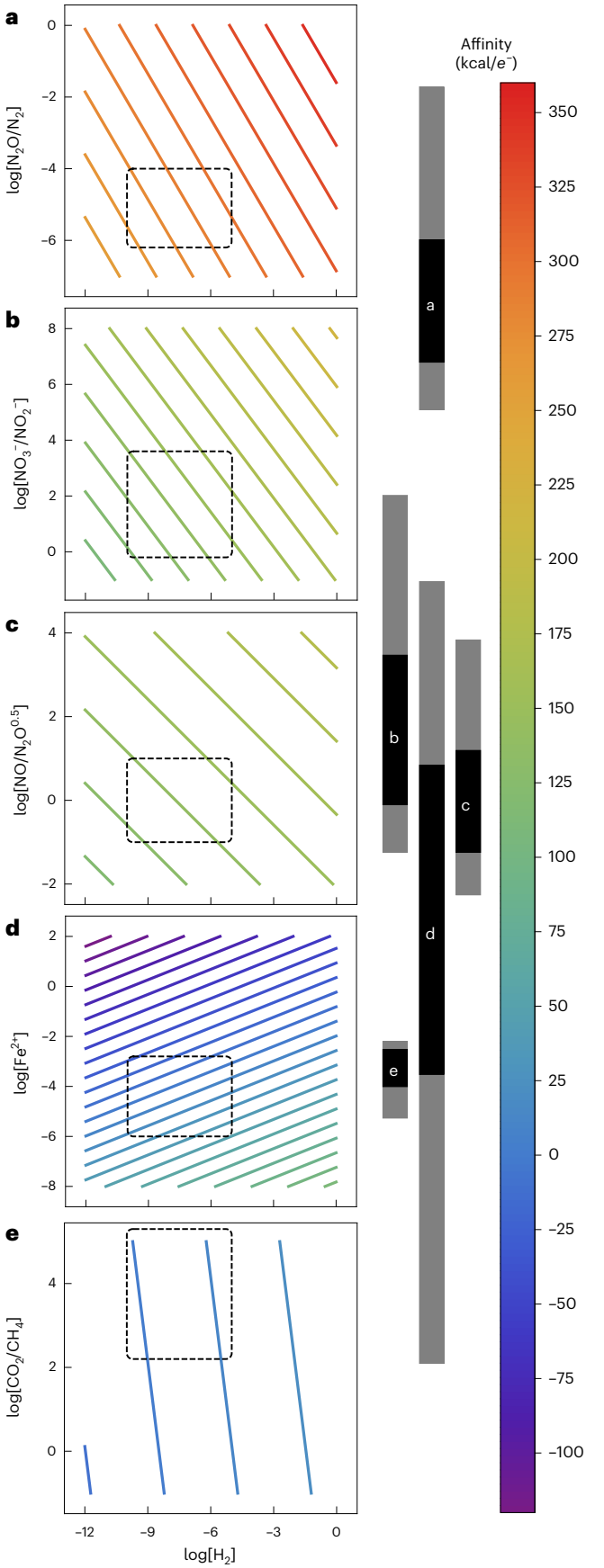

Fig. 4 | Affinity landscapes. a, Reduction of N_2O gas by molecular hydrogen (H_2). **b**, Reduction of NO_3^- by H_2. **c**, Reduction of NO by H_2. **d**, Magnetite reduction by H_2 at pH 7.3. **e**, CO_2 reduction by H_2 (methanogenesis). The coloured curves in each plot represent lines of constant affinity, set 10 kcal apart. The black boxes represent regions of probable species activities (that is, each of these regions is aligned on the scale bar to the right for easier comparison between reactions). More details of the reaction stoichiometry are provided in the Supplementary Information.

mineral-catalysed reduction of NO_2^- is several orders of magnitude faster than photo-reduction of NO_2^- (ref. [4]), reaction on Fe mineral surfaces constituted a sink for fixed nitrogen from both the NO_3^- and NO_2^- pool. We henceforth tested whether NO_2^- consumption on mineral particles and in sediments exhausted seawater NO_2^-, possibly impeding mineral-catalysed NO and N_2O production (Supplementary Information). Assuming a combined NO_x flux of 2.5×10^{11} mol N yr^{-1} from lightning events[40], volcanic eruptions[41] and meteoritic impacts[42], GR particle surfaces equivalent to 200% those of Kabuno Bay draw the NO_2^- concentration down to 8.4 µM. At higher GR abundances, the reactants became exhausted and any NO_2^- from NO_3^- photo-reduction or deposited to the ocean directly converted to NO and N_2O. Importantly, abiotic fluxes were co-regulated by the influx of NO_x into the ocean and the amount of GR suspended in seawater. If N_2O formation decreased due to reactant limitation, atmospheric N_2O may have reached sub-ppb concentrations, but no lower than HNO-derived N_2O concentrations (>0.5 ppb; Fig. 3).

Effects of NO and N_2O on early anaerobic microbial life

With the assumption that individual denitrification steps evolved consecutively, our results provide a geochemical explanation for biochemical patterns known for over three decades. A primitive form of NO and N_2O reduction probably preceded aerobic respiration based on the structural resemblance of NO[43] and N_2O[44–46] reductases with components of cytochrome c oxidase, including hydrogen bond and metal configuration, Ca ligation[47] and phylogenetic analyses[43,48]. This concept is supported by a simple make-up of the respiratory chains involving quinone-dependent NO reductase and membrane-bound N_2O reductases, as present in some Gram$^+$ bacteria[45,46]. Because of their dependence on a complex cytochrome c maturation system, NO_3^- and NO_2^- reductases probably evolved later[45].

To constrain the effects of N_2O on early microorganisms, we estimated dissolved abundances based on atmosphere-to-seawater diffusion. Accordingly, at least 0.04–4.70 nM N_2O was dissolved in the ferruginous seawater based on mere equilibration with the Archaean air without haze (Supplementary Table 4). True concentrations were probably higher in proximity around actively N_2O-generating GR particles. Contemporary microbial N_2O consumption is based on high-affinity enzymes adapted to low N_2O steady-state concentrations[49]. For example, 30 nM N_2O is readily metabolized in anoxic seawater[20], but the minimum threshold for marine N_2O respiration is probably much lower (S. Yoon, personal communication).

Under generally accepted Archaean ocean conditions, N_2O reduction to N_2 is thermodynamically favourable but kinetically hindered without enzymatic catalysis, making it an ideal potential energy source. For instance, coupled to H_2 oxidation (H_2 as a simple and available reductant), an affinity of up to 300 kcal per electron accepted by N_2O is significantly higher than that of any other redox reaction tested. Moreover, GR shuttling may have been effective for NO molecules to reach benthic microbial life, acting as a biological electron sink[43]. The availability of NO was essential for early denitrifying microorganisms because marine sediments in the Archaean lacked nitrification as a source of NO_x. The reduction of the available NO_x (Fig. 4a–c) achieves a higher energy yield than magnetite reduction (Fig. 4d) and methanogenesis (Fig. 4e), underscoring their benefit to microbial life in a sulfate-poor marine environment.

https://doi.org/10.1038/s41561-022-01089-9

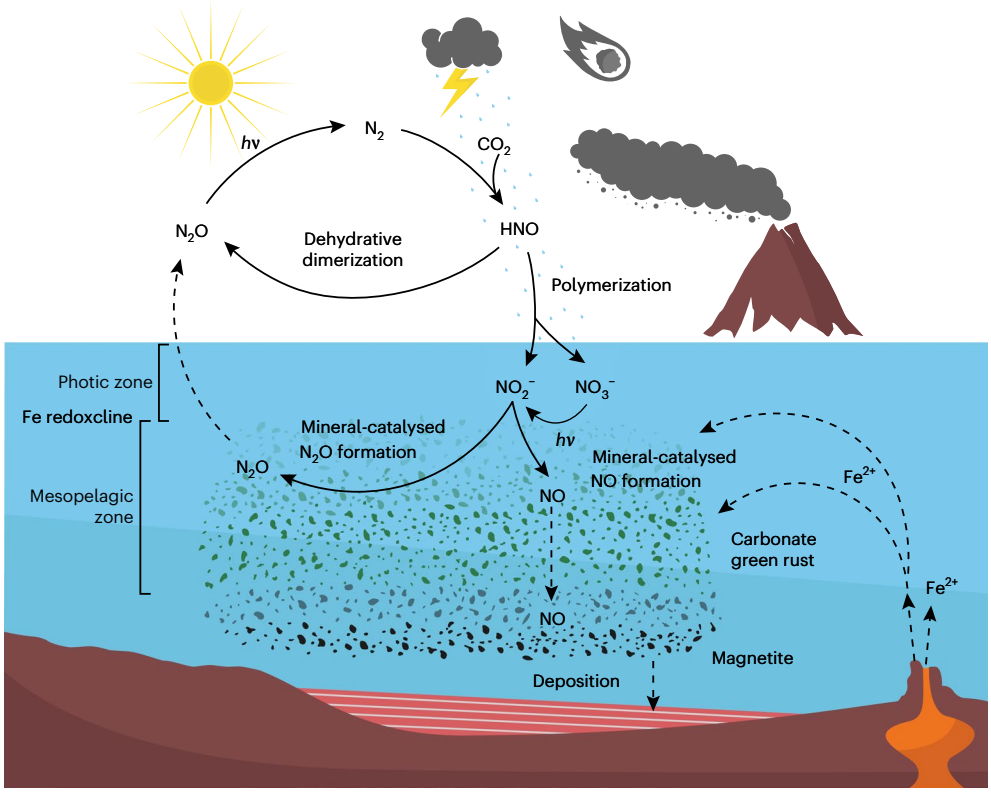

Fig. 5 | Schematic of mineral-catalysed NO and N_2O formation at the junction of the early nitrogen and iron cycle. Heat shock reactions, as stimulated by galactic cosmic rays, meteoritic impact plumes and volcanic and thunderstorm lightening, produced the central precursor HNO, which dimerized directly to N_2O or polymerized into NO_2^- and NO_3^- (ref. [34]). These nitrogen oxides became interspersed into the surface ocean as plumes by rainout. Any NO_3^- constituted a source of NO_2^- through photo-reduction[4]. Upwelling Fe^{2+} precipitated into Fe oxyhydroxides and green rust in the Fe redoxcline. Driven by Fe mineral catalysis, NO_2^- was reduced to N_2O. The abiotic nitrogen cycle was closed by photolytic destruction of emitted N_2O to N_2. As a byproduct, NO molecules remained bound at mineral particles as nitrosyl. This way, green rust may have served as an NO shuttle enabling transport into the deep ocean. Sinking green rust transformed into Fe^{2+} carbonates, Fe^{2+} silicates and magnetite, which then were deposited. The dashed lines mark diffusive or gravitational transport, whereas solid lines indicate chemical reactions. Adapted from ref. [67].

Conversely, NO and N_2O could have been damaging to microorganisms. The inhibitory effects of the NO molecule are caused by radical production and nitrosative stress[50], which forced microbial cells to rapidly reduce NO using NO reductase-type enzymes. Given the negative effects of NO on phototrophs[51,52] (15 nM NO halted growth), mineral-catalysed NO formation could have corrupted the capability of phototrophic communities to harvest light energy. In contrast with its energetic benefits, N_2O can bind and inactivate vitamin B_{12}[53,54]. Among diverse roles as cofactor in essential cellular processes, vitamin B_{12} is a key metabolite for methanogens because its cobalt(I) centre serves as a methyl acceptor during methanol-to-methane transformation[55]. For example, methanogens in tropical soils have shown metabolic sensitivity to N_2O as low as 4 nM[56], which could have feasibly accumulated in ferruginous waters (Supplementary Table 4). Whether NO and N_2O had positive or negative net effects on early microorganisms remains elusive but, in either case, a mineral source of these compounds inevitably exerted selective pressure and shaped the composition of Archaean microbial communities.

Our study suggests that a considerable portion of NO_x^- in the ferruginous Archaean ocean was diverted to NO and N_2O, leading to more oxidized products compared with other sink pathways (ending in N_2 or ammonia). Given GR phases at 100% Kabuno Bay equivalence, low seawater NO_2^- levels and a 70% ocean cover of Earth's surface, N_2O emissions exported 2.1 TgN yr^{-1} into the Archaean atmosphere. We regard any biological N_2O production (for example, through ammonia oxidation) that would have added to this flux as trivial in the reducing milieu of a ferruginous ocean. Substantial amounts of mineral surface-bound NO could have been transported down to the seafloor by the settling of GR precipitates. Assuming a particle sinking velocity of 50 m d^{-1} (ref. [57]), 1.2 TgN yr^{-1} in the form of NO could have reached ocean sediments. Thus, the degree of thermodynamic disequilibria in the redox balance of the Archaean nitrogen cycle may have been underestimated[58]. We also caution to use N_2O as a unique biosignature in exoplanet exploration. It is possible that conditions for the mineral-catalysed N_2O production on early Earth-like exoplanets are even more favourable, resulting in N_2O atmospheric concentrations exceeding modern ones (higher abiotic nitrogen fixation rates and a higher Fe mineral load). Signals from low-methane atmospheres could be interpreted as false positives without any biological basis.

We provide evidence that higher O_3 levels are not required to reach ppb N_2O concentrations before the GOE and present a concept of a complete abiotic N_2O cycle closed by mineral-catalysed reactions (Fig. 5), hundreds of millions of years before the biological and more efficient production and consumption of N_2O[11]. Although the effects of abiotic N_2O production on the early climate were probably modest, marine sources of NO and N_2O could have notably influenced the evolution and survival strategies of Archaean life. Rather than being a mainly biological invention, the reduced branch of the abiotic nitrogen cycle, driven by chemical kinetics highly similar to those of modern enzymatically mediated conversions (Table 1), was seemingly co-opted by early organisms.

Online content

Any methods, additional references, Nature Portfolio reporting summaries, source data, extended data, supplementary information,

acknowledgements, peer review information; details of author contributions and competing interests; and statements of data and code availability are available at https://doi.org/10.1038/s41561-022-01089-9.

References

1. Mancinelli, R. L. & McKay, C. P. The evolution of nitrogen cycling. *Orig. Life Evol. Biosph.* **18**, 311–325 (1988).
2. Wong, M. L., Charnay, B. D., Gao, P., Yung, Y. L. & Russell, M. J. Nitrogen oxides in early Earth's atmosphere as electron acceptors for life's emergence. *Astrobiology* **17**, 975–983 (2017).
3. Summers, D. P. & Khare, B. Nitrogen fixation on early Mars and other terrestrial planets: experimental demonstration of abiotic fixation reactions to nitrite and nitrate. *Astrobiology* **7**, 333–341 (2007).
4. Ranjan, S., Todd, Z. R., Rimmer, P. B., Sasselov, D. D. & Babbin, A. R. Nitrogen oxide concentrations in natural waters on early Earth. *Geochem. Geophys. Geosystems* **20**, 2021–2039 (2019).
5. Kampschreur, M. J., Kleerebezem, R., de Vet, W. W. J. M. & Loosdrecht, M. C. M. V. Reduced iron induced nitric oxide and nitrous oxide emission. *Water Res.* **45**, 5945–5952 (2011).
6. Jones, L. C., Peters, B., Pacheco, J. S. L., Casciotti, K. L. & Fendorf, S. Stable isotopes and iron oxide mineral products as markers of chemodenitrification. *Environ. Sci. Technol.* **49**, 3444–3452 (2015).
7. Grabb, K. C., Buchwald, C., Hansel, C. M. & Wankel, S. D. A dual nitrite isotopic investigation of chemodenitrification by mineral-associated Fe(II) and its production of nitrous oxide. *Geochim. Cosmochim. Acta* **196**, 388–402 (2017).
8. Kasting, J. F. in *Earth's Early Atmosphere and Surface Environment* 19–28 (Geological Society of America, 2014).
9. Gough, D. O. in *Physics of Solar Variations* 21–34 (Springer Dordrecht, 1981).
10. Stanton, C. L. et al. Nitrous oxide from chemodenitrification: a possible missing link in the Proterozoic greenhouse and the evolution of aerobic respiration. *Geobiology* **16**, 597–609 (2018).
11. Buick, R. Did the Proterozoic 'Canfield Ocean' cause a laughing gas greenhouse? *Geobiology* **5**, 97–100 (2007).
12. Godfrey, L. V. & Falkowski, P. G. The cycling and redox state of nitrogen in the Archaean ocean. *Nat. Geosci.* **2**, 725–729 (2009).
13. Roberson, A. L., Roadt, J., Halevy, I. & Kasting, J. F. Greenhouse warming by nitrous oxide and methane in the Proterozoic Eon. *Geobiology* **9**, 313–320 (2011).
14. Li, Y., Yamaguchi, A., Yamamoto, M., Takai, K. & Nakamura, R. Molybdenum sulfide: a bioinspired electrocatalyst for dissimilatory ammonia synthesis with geoelectrical current. *J. Phys. Chem. C* **121**, 2154–2164 (2017).
15. Halevy, I., Alesker, M., Schuster, E. M., Popovitz-Biro, R. & Feldman, Y. A key role for green rust in the Precambrian oceans and the genesis of iron formations. *Nat. Geosci.* **10**, 135–139 (2017).
16. Sorensen, J. & Thorling, L. Stimulation by lepidocrocite (7-FeOOH) of Fe(II)-dependent nitrite reduction. *Geochim. Cosmochim. Acta* **55**, 1289–1294 (1991).
17. Hansen, H., Borggaard, O. K. & Sorensen, J. Evaluation of the free energy of formation of Fe(II)–Fe(III) hydroxide-sulphate (green rust) and its reduction of nitrite. *Geochim. Cosmochim. Acta* **58**, 2599–2608 (1994).
18. Ottley, C. J., Davison, W. & Edmunds, W. M. Chemical catalysis of nitrate reduction by iron (II). *Geochim. Cosmochim. Acta* **61**, 1819–1828 (1997).
19. Zegeye, A. et al. Green rust formation controls nutrient availability in a ferruginous water column. *Geology* **40**, 599–602 (2012).
20. Babbin, A. R., Bianchi, D., Jayakumar, A. & Ward, B. B. Rapid nitrous oxide cycling in the suboxic ocean. *Science* **348**, 1127–1129 (2015).
21. Ji, Q., Babbin, A. R., Jayakumar, A., Oleynik, S. & Ward, B. B. Nitrous oxide production by nitrification and denitrification in the Eastern Tropical South Pacific oxygen minimum zone. *Geophys. Res. Lett.* **42**, 10755–10764 (2015).
22. Gordon, A. D. et al. Reduction of nitrite and nitrate on nano-dimensioned FeS. *Orig. Life Evol. Biosph.* **43**, 305–322 (2013).
23. Llirós, M. et al. Pelagic photoferrotrophy and iron cycling in a modern ferruginous basin. *Sci. Rep.* **5**, 13803 (2015).
24. Swanner, E. D. et al. Modulation of oxygen production in Archaean oceans by episodes of Fe(II) toxicity. *Nat. Geosci.* **8**, 126–130 (2015).
25. Sumner, D. Y. Carbonate precipitation and oxygen stratification in late Archean seawater as deduced from facies and stratigraphy of the Gamohaan and Frisco formations, Transvaal Supergroup, South Africa. *Am. J. Sci.* **297**, 455–487 (1997).
26. Sumner, D. Y. & Grotzinger, J. P. Were kinetics of Archean calcium carbonate precipitation related to oxygen concentration? *Geology* **24**, 119–122 (1996).
27. Battaglia, G. & Joos, F. Marine N_2O emissions from nitrification and denitrification constrained by modern observations and projected in multimillennial global warming simulations. *Glob. Biogeochem. Cycles* **32**, 92–121 (2018).
28. Hu, R., Seager, S. & Bains, W. Photochemistry in terrestrial exoplanet atmospheres. I. Photochemistry model and benchmark cases. *Astrophys J.* **761**, 166 (2012).
29. Kaiser, J., Röckmann, T., Brenninkmeijer, C. A. M. & Crutzen, P. J. Wavelength dependence of isotope fractionation in N_2O photolysis. *Atmos. Chem. Phys.* **3**, 303–313 (2003).
30. Airapetian, V. S., Glocer, A., Gronoff, G., Hebrard, G. & Danchi, W. Prebiotic chemistry and atmospheric warming of early Earth by an active young Sun. *Nat. Geosci.* **9**, 452–455 (2016).
31. Wolf, E. T. & Toon, O. B. Fractal organic hazes provided an ultraviolet shield for early Earth. *Science* **328**, 1266–1268 (2010).
32. Catling, D. C., Zahnle, K. J. & McKay, C. P. Biogenic methane, hydrogen escape, and the irreversible oxidation of early Earth. *Science* **293**, 839–843 (2001).
33. Laneuville, M., Kameya, M. & Cleaves, H. J. Earth without life: a systems model of a global abiotic nitrogen cycle. *Astrobiology* **18**, 897–914 (2018).
34. Hu, R. & Diaz, H. D. Stability of nitrogen in planetary atmospheres in contact with liquid water. *Astrophys J.* **886**, 126 (2019).
35. Saito, M. A. et al. Abundant nitrite-oxidizing metalloenzymes in the mesopelagic zone of the tropical Pacific Ocean. *Nat. Geosci.* **13**, 355–362 (2020).
36. Summers, D. P. & Chang, S. Prebiotic ammonia from reduction of nitrite by iron (II) on the early Earth. *Nature* **365**, 630–633 (1993).
37. Brandes, J. A. et al. Abiotic nitrogen reduction on the early Earth. *Nature* **395**, 365–367 (1998).
38. Nishizawa, M. et al. Stable abiotic production of ammonia from nitrate in komatiite-hosted hydrothermal systems in the Hadean and Archean oceans. *Minerals* **11**, 321 (2021).
39. Halevy, I. & Bachan, A. The geologic history of seawater pH. *Science* **355**, 1069–1071 (2017).
40. Harman, C. E. et al. Abiotic O_2 levels on planets around F, G, K, and M stars: effects of lightning-produced catalysts in eliminating oxygen false positives. *Astrophys J.* **866**, 56 (2018).
41. Mather, T. A., Pyle, D. M. & Allen, A. G. Volcanic source for fixed nitrogen in the early Earth's atmosphere. *Geology* **32**, 905–908 (2004).
42. Kasting, J. F. Bolide impacts and the oxidation state of carbon in the Earth's early atmosphere. *Orig. Life Evol. Biosph.* **20**, 199–231 (1990).
43. Ducluzeau, A.-L. et al. Was nitric oxide the first deep electron sink? *Trends Biochem. Sci.* **34**, 9–15 (2009).

44. Viebrock, A. & Zumft, W. G. Molecular cloning, heterologous expression, and primary structure of the structural gene for the copper enzyme nitrous oxide reductase from denitrifying *Pseudomonas stutzeri*. *J. Bacteriol.* **170**, 4658–4668 (1988).
45. Chen, J. & Strous, M. Denitrification and aerobic respiration, hybrid electron transport chains and co-evolution. *Biochim. Biophys. Acta Bioenerg.* **1827**, 136–144 (2013).
46. Suharti, S. & de Vries, S. Membrane-bound denitrification in the Gram-positive bacterium *Bacillus azotoformans*. *Biochem. Soc. Trans.* **33**, 130–133 (2005).
47. Saraste, M. & Castresana, J. Cytochrome oxidase evolved by tinkering with denitrification enzymes. *FEBS Lett.* **341**, 1–4 (1994).
48. Sousa, F. L. et al. The superfamily of heme–copper oxygen reductases: types and evolutionary considerations. *Biochim. Biophys. Acta Bioenerg.* **1817**, 629–637 (2012).
49. Yoon, S. et al. Nitrous oxide reduction kinetics distinguish bacteria harboring clade I NosZ from those harboring clade II NosZ. *Appl. Environ. Microbiol.* **82**, 3793–3800 (2016).
50. Heinrich, T. A. et al. Biological nitric oxide signalling: chemistry and terminology. *Br. J. Pharmacol.* **169**, 1417–1429 (2013).
51. Santana, M. M., Gonzalez, J. M. & Cruz, C. Nitric oxide accumulation: the evolutionary trigger for phytopathogenesis. *Front. Microbiol.* **8**, 1947 (2017).
52. Nikeleit, V. et al. Inhibition of photoferrotrophy by nitric oxide in ferruginous environments. Preprint at *EarthArXiv* https://doi.org/10.31223/X5XS60 (2021).
53. Drummond, J. T. & Matthews, R. G. Nitrous oxide degradation by cobalamin-dependent methionine synthase: characterization of the reactants and products in the inactivation reaction. *Biochemistry* **33**, 3732–3741 (1994).
54. Drummond, J. T. & Matthews, R. G. Nitrous oxide inactivation of cobalamin-dependent methionine synthase from *Escherichia coli*: characterization of the damage to the enzyme and prosthetic group. *Biochemistry* **33**, 3742–3750 (1994).
55. Matthews, R. G. Cobalamin-dependent methyltransferases. *Acc. Chem. Res.* **34**, 681–689 (2001).
56. Buessecker, S. et al. Microbial communities and interactions of nitrogen oxides with methanogenesis in diverse peatlands of the Amazon basin. *Front. Microbiol.* **12**, 659079 (2021).
57. McDonnell, A. M. P. & Buesseler, K. O. Variability in the average sinking velocity of marine particles. *Limnol. Oceanogr.* **55**, 2085–2096 (2010).
58. Krissansen-Totton, J., Olson, S. & Catling, D. C. Disequilibrium biosignatures over Earth history and implications for detecting exoplanet life. *Sci. Adv.* **4**, eaao5747 (2018).
59. Nicholls, J. C., Davies, C. A. & Trimmer, M. High-resolution profiles and nitrogen isotope tracing reveal a dominant source of nitrous oxide and multiple pathways of nitrogen gas formation in the central Arabian Sea. *Limnol. Oceanogr.* **52**, 156–168 (2007).
60. Dalsgaard, T., Thamdrup, B., Farías, L. & Revsbech, N. P. Anammox and denitrification in the oxygen minimum zone of the eastern South Pacific. *Limnol. Oceanogr.* **57**, 1331–1346 (2012).
61. Löscher, C. R. et al. Production of oceanic nitrous oxide by ammonia-oxidizing archaea. *Biogeosciences* **9**, 2419–2429 (2012).
62. Bourbonnais, A. et al. N_2O production and consumption from stable isotopic and concentration data in the Peruvian coastal upwelling system. *Glob. Biogeochem. Cycles* **31**, 678–698 (2017).
63. Frame, C. H. & Casciotti, K. L. Biogeochemical controls and isotopic signatures of nitrous oxide production by a marine ammonia-oxidizing bacterium. *Biogeosciences* **7**, 2695–2709 (2010).
64. Zafiriou, O. C. & McFarland, M. Nitric oxide from nitrite photolysis in the central equatorial Pacific. *J. Geophys. Res. Atmos.* **86**, 3173–3182 (1981).
65. Liu, C.-Y. et al. Determination of dissolved nitric oxide in coastal waters of the Yellow Sea off Qingdao. *Ocean Sci.* **13**, 623–632 (2017).
66. Martens-Habbena, W. et al. The production of nitric oxide by marine ammonia-oxidizing archaea and inhibition of archaeal ammonia oxidation by a nitric oxide scavenger. *Environ. Microbiol.* **17**, 2261–2274 (2015).
67. Li, Y.-L., Konhauser, K. O. & Zhai, M. The formation of primary magnetite in the early Archean oceans. *Earth Planet. Sci. Lett.* **466**, 103–114 (2017).

Methods

Mineral synthesis

Carbonate GR was synthesized according to the following. In brief, 18.2 MΩ·cm water was made anoxic by boiling and sparging with CO_2/N_2 (20:80). An anoxic 0.4 M Fe^{2+}/Fe^{3+} solution (0.1 l) was prepared by mixing 7.42 g $FeSO_4 \cdot 7\ H_2O$ (>99%; Sigma–Aldrich) and 2.66 g anhydrous $Fe_2(SO_4)_3$ (97%; Sigma–Aldrich). An alkaline, anoxic solution of 0.466 M Na_2CO_3 (Thermo Fisher Scientific) in 0.8 M NaOH (Thermo Fisher Scientific) (0.1 l) was prepared by dissolving NaOH first under a constant stream of CO_2/N_2 gas, after which Na_2CO_3 was added. Both solutions were stirred continuously at 500 r.p.m. The alkaline solution was injected into the Fe^{2+}/Fe^{3+} solution using CO_2/N_2 flushed syringes. Precipitation occurred immediately and the suspension was stirred in the dark for 24 h. Magnetite was synthesized as nanoparticles following previously described protocols[68,69].

Mineral harvest

GR and magnetite precipitates were washed in an anaerobic chamber (0.5% H_2 in N_2; Coy Laboratory Products) using a vacuum filtration unit (130-4020; Nalgene) and 0.45 µm cellulose acetate filter membranes (Sartorius). Anoxic 18.2 MΩ·cm water was poured onto the precipitates for a minimum of eight cycles (pouring followed by extracting water). When the filtrate flow decreased to a minimum, the wet mineral paste was removed from the filter. Wet carbonate GR (73.8% water content) and wet magnetite (47.2% water content) were added to microcosms. The wet minerals were also used for mineralogical characterization by X-ray diffraction (XRD) and microscopy. For Brunauer–Emmett–Teller (BET) analysis, a defined amount of precipitate was dried in small boxes filled with drierite and placed into the anaerobic chamber. The dry weight was constant after 3–5 d.

XRD

Powder XRD was conducted on a subset of samples after synthesis and washing of the mineral products. A glycerol smear was prepared with 10 mg sample in the anaerobic chamber and sealed in a glass vial to prevent oxidation before analysis. To collect the XRD data, the sample was removed from the vial and spread across a quartz zero background plate that was placed onto a horizontal stage in a Bruker D-5000 diffractometer equipped with a Copper Kα X-ray tube (30 kV; λ = 1.791 Å). Signal peaks were compared to reference diffractograms in the RRUFF database. Instrument broadening was determined by a standard polycrystalline alumina sample. XRD data were analysed with the CrystalDiffract software version 6.8.2 for Mac.

Scanning and transmission electron microscopy

Samples for scanning electron microscopy (SEM) imaging were mounted on aluminium pin stubs with double-sided carbon tabs in a glove box and transported in a sealed jar under an anoxic atmosphere to the microscope. Samples were not sputter coated. Images were taken on an XL30 ESEM FEG (Philips) operated at a 30 kV accelerating voltage and a 21 pA beam current. Transmission electron microscopy (TEM) samples were dispersed on a Lacey Carbon film using 200 mesh copper grids. The instrument used was a CM200 Field Emission Microscope at 200 kV (Philips) with a spherical aberration coefficient C_s = 1.2 mm and a point-to-point resolution of 0.25 nm. Imaging was done on a Gatan Orius CCD system.

BET surface area measurements

For analysis of the BET surface area, dried mineral precipitate was weighed inside the anaerobic chamber and added to a Florence glass flask that was closed with a rubber stopper for transport to the instrument. The BET surface in replicate samples (n = 3 for GR and n = 2 for magnetite) was quantified using N_2 gas on a TriStar II 3020 analyzer (Micromeritics). The instrument has a limit of detection of 1 m^2. Our results (Supplementary Table 4) are roughly consistent with previously determined BET values of 47 $m^2\ g^{-1}$ for GR[70] and 95 $m^2\ g^{-1}$ for magnetite[71].

We performed calculations of the mineral surface area for both minerals to supplement our measurements. To derive the mineral density, we calculated the average crystallite size by inserting the full width at half maximum, as determined from the diffractograms and the Bragg angle of the GR 0 0 3 reflection and of the magnetite 3 1 1 reflection, into the Scherrer equation. The mineral density was calculated using the formula $\rho = (M \times Z)/(V_c \times 0.60225)$, where M is molar mass, Z is the number of molecules per crystallite and V_c is the crystallite size. The density and grain volume, as measured by TEM/SEM. were used to calculate the grain mass. The final value in $m^2\ g^{-1}$ was derived from the grain mass and the grain surface area (TEM/SEM). For magnetite, we calculated a surface area of 88.8 $m^2\ g^{-1}$. For GR, we calculated a minimum approximation (surface of GR sheets only) of 27.6 $m^2\ g^{-1}$ and a maximum approximation (including the surface between sheets) of 538.5 $m^2\ g^{-1}$. Thus, our measured value for magnetite is somewhat lower than the calculated and literature value. The measured value for GR is in good agreement with the literature value and at the lower end of the calculated range.

Incubation conditions

Interactions of nitrogen oxides with Fe minerals were tested in anoxic microcosms designed to mimic Archaean ocean conditions as closely as possible. Borosilicate glass bottles (30–120 ml) were closed with thick butyl rubber stoppers and a headspace of 20% CO_2 in N_2 was used throughout the experiment. All glassware was washed with 2 M HCl before use. The liquid phase constituted one-third of the microcosm total volume. We used a published recipe for artificial Archaean seawater[72] and omitted any sulfur species (0.56 M NaCl and 0.01 M $NaHCO_3$). The pH was initially set to 7.3 using a CO_2–HCO_3^- buffer. We boiled 18.2 MΩ·cm water and sparged it with CO_2/N_2 (20:80) while it was cooling on ice. Salts were added during the sparging. The anoxic solution was then dispensed with a pipetor into microcosms in an anaerobic chamber (0.5% H_2 in N_2; Coy Laboratory Products). Nitrate and nitrite stock solutions were prepared with their respective sodium salts, $NaNO_3$ (≥99%; Thermo Fisher Scientific) and $NaNO_2$ (≥97%; Acros Organics) and dissolved in artificial seawater. The solutions were then sparged with N_2 and filter sterilized (0.8/0.2 µm pore seize; VWR) in the anaerobic chamber. Controls with aqueous Fe^{2+} were prepared in anoxic artificial seawater and $FeCl_2$ (≥99%; Thermo Fisher Scientific). The mineral surface area was controlled by the mineral mass added. Wet minerals were weighed in the anaerobic chamber and distributed into microcosms using ethanol-washed plastic spatulas. Before the start of the incubations with the injection of the NO_x^- solution, mineral agglomerates were dissipated in an ultrasonic bath (Ultrasonic Cleaner 2510; Branson Ultrasonics). Microcosms were shaken at 250 r.p.m. in the dark and at room temperature for the entire duration of the experiment. Controls were incubated in the anaerobic chamber to test for potential leaking through stoppers, which did not occur. To dissolve mineral particles during incubations, 1.6 ml concentrated 12 N HCl or 37 N H_2SO_4 was slowly injected through bottle septa to 10 ml mineral–seawater suspension. Dissolution of solid particles occurred instantly and the liquid first turned turbid orange-green and then clear green-yellow (HCl) or light yellow (H_2SO_4) within 15–20 h. The last measurement of NO in the headspace was taken when the liquid was clear (Supplementary Fig. 5).

Dissolved nitrite, nitrate, ammonium, ferrous and ferric iron measurements

All dissolved analytes were quantified spectrometrically with plate assays. Nitrite in solution was quantified with the Griess Reagent (G2930; Promega). Nitrate was first reduced to nitrite by vanadium(III) chloride and then quantified as nitrite[73]. Ammonium production was verified with the salicylic acid assay[74]. To determine the Fe^{2+}/Fe^{3+}

solid-phase ratio, mineral particles were settled, after which supernatant artificial seawater was removed from the microcosms. Anoxic acidic extraction of GR and magnetite was conducted by completely dissolving mineral samples in 6 M HCl, followed by incubation at 70 °C for 24 h under 100% N_2 headspace to prevent abiotic oxidation[68]. The samples were then further diluted 1:10 in 1 M HCl. Ferrous and ferric ions in the extracts were measured by reaction with ferrozine following the method of Stookey[75].

N_2O gas measurements

To quantify N_2O production, 200 µl headspace gas was sampled with a gas-tight syringe (VICI Precision Sampling) and injected into a gas chromatograph (SRI Instruments) equipped with an electron-capture detector (ECD). Two continuous HayeSep D columns were kept at 90 °C (oven temperature) and N_2 (UHP grade 99.999%; Praxair) was used as the carrier gas. The ECD current was 250 mV and the ECD cell was kept at 350 °C. The N_2O measurements were calibrated using customized standard mixtures (Scott Specialty Gases; accuracy ±5%) over a range of 0.25–100 parts per million by volume. Gas accumulation in the microcosms was monitored over time. Gas concentrations were corrected using Henry's law and the dimensionless concentration constant $k_H^{cc}(N_2O) = 0.6112$ to account for gas partitioning into the aqueous phase at 25 °C.

NO gas measurements

NO was quantified in the microcosm headspace with a chemiluminescence-based analyzer (LMA-3D NO_2 analyzer; Unisearch Associates). Headspace gas (50 µl) was withdrawn with a CO_2–N_2-flushed gas-tight syringe and injected into the analyzer. The injection port was customized to fit the injection volume and consisted of a T-junction with an air filter at one end and a septum at the other end. An internal pump generated a consistent airflow. In short, sample NO was oxidized to NO_2 by a CrO_3 catalyst. The NO_2 flew across a fabric wick saturated with a Luminol solution. Luminol was obtained from Drummond Technology (Canada). Readings were corrected for background NO_2 every 15 min (zeroing). The shell airflow rate was kept at 500 ml min^{-1} and the span potentiometer was set to 8. Measurements were calibrated with a 0.1 ppm NO (in N_2) standard (<0.0005 ppm NO_2; Scott-Marin) over a range of 5–1,000 parts per billion by volume. Gas concentrations were corrected using Henry's law and the dimensionless concentration constant $k_H^{cc}(NO) = 0.0465$ to account for gas partitioning into the aqueous phase at 25 °C.

Flux modelling

The partial fluxes of the overall flux balance $\Phi_{sed} + \Phi_{par} = \Phi_{atm}$ were normalized to a 100 m vertical slab with 1 m^2 basis. The upper 100 m ocean water is typically considered to be well mixed; hence, reactant and catalyst are homogeneously distributed in that space. Depending on the water depth, a portion of the NO_x could reach the ocean floor, which is why we added a generic sediment flux (Φ_{sed}) to the balance equation. The dominant flux would emerge from floating GR mineral particles (Φ_{par}) that are distributed along the water column. For simplicity, we assume that all GR had aged into magnetite in the sediment and all floating particles were GR phases. We refer to the Supplementary Information for a more detailed description of the derivation of the partial fluxes, the error propagation method and thermodynamic calculations.

Photochemical modelling

We have used an atmospheric photochemistry model to simulate the effects of N_2O emission into an anoxic atmosphere akin to that of the Archaean Earth's. The photochemistry model used[28,76] has been validated by computing the atmospheric compositions of present-day Earth and Mars, as the outputs agreed with the observations of major trace gases in Earth's and Mars' atmospheres[77]. For example, Fig. 2-2 of ref. [77] shows that the model reproduces the vertical profile of the mixing ratio of N_2O in modern Earth's atmosphere using a globally averaged emission rate (1×10^9 molecules per cm per s). For this work, we simulate a 1-bar atmosphere of 95% N_2 and 5% CO_2 to approximate the anoxic and CO_2-rich environment of the Archaean Earth[78]. We used the ultraviolet and optical spectrum of the present-day Sun to drive the photochemical model because the solar flux in 200–230 nm, which causes the photodissociation of N_2O, depends weakly on the age[79]. We have updated the absorption cross-sections of CO_2 and H_2O using the latest experimental results[80]. We assume a surface temperature of 288 K and a stratospheric temperature of 200 K, and adopt the eddy diffusion coefficient derived from the number density profiles of trace gases on Earth[81]. The photochemistry model includes a comprehensive reaction network for O, H, C, N and S species, including sulfur and sulfuric acid aerosols, and includes volcanic outgassing of CO, H_2, SO_2 and H_2S. The outgassing rate is not high enough to produce an H_2SO_4 aerosol layer in the atmosphere and these gases do not impact the lifetime of N_2O significantly.

Data availability

All of the data relating to this manuscript are provided within the manuscript and its Supplementary Information and are available as raw data on the Figshare platform (https://doi.org/10.6084/m9.figshare.20740204.v3) or upon request from the corresponding author.

Code availability

The code for the photochemical model will be shared by the corresponding author upon request.

References

68. Byrne, J. M. et al. Redox cycling of Fe(II) and Fe(III) in magnetite by Fe-metabolizing bacteria. *Science* **347**, 1473–1476 (2015).
69. Pearce, C. I. et al. Synthesis and properties of titanomagnetite ($Fe_{3-x}Ti_xO_4$) nanoparticles: a tunable solid-state Fe(II/III) redox system. *J. Colloid Interface Sci.* **387**, 24–38 (2012).
70. Williams, A. G. B. & Scherer, M. M. Kinetics of Cr(VI) reduction by carbonate green rust. *Environ. Sci. Technol.* **35**, 3488–3494 (2001).
71. Sun, Z.-X., Su, F.-W., Forsling, W. & Samskog, P.-O. Surface characteristics of magnetite in aqueous suspension. *J. Colloid Interface Sci.* **197**, 151–159 (1998).
72. Anbar, A. D. & Holland, H. D. The photochemistry of manganese and the origin of banded iron formations. *Geochim. Cosmochim. Acta* **56**, 2595–2603 (1992).
73. Miranda, K. M., Espey, M. G. & Wink, D. A. A rapid, simple spectrophotometric method for simultaneous detection of nitrate and nitrite. *Nitric Oxide* **5**, 62–71 (2001).
74. Kandeler, E. & Gerber, H. Short-term assay of soil urease activity using colorimetric determination of ammonium. *Biol. Fertil. Soils* **6**, 68–72 (1988).
75. Stookey, L. L. Ferrozine—a new spectrophotometric reagent for iron. *Anal. Chem.* **42**, 779–781 (1970).
76. Hu, R., Seager, S. & Bains, W. Photochemistry in terrestrial exoplanet atmospheres. II. H_2S and SO_2 photochemistry in anoxic atmospheres. *Astrophys. J.* **769**, 6 (2013).
77. Hu, R. Atmospheric photochemistry, surface features, and potential biosignature gases of terrestrial exoplanets. PhD thesis, Massachusetts Institute of Technology (2013).
78. Catling, D. C. & Zahnle, K. J. The Archean atmosphere. *Sci. Adv.* **6**, eaax1420 (2020).
79. Claire, M. W. et al. The evolution of solar flux from 0.1 nm to 160 µm: quantitative estimates for planetary studies. *Astrophys. J.* **757**, 95 (2012).
80. Ranjan, S. et al. Photochemistry of anoxic abiotic habitable planet atmospheres: impact of new H_2O cross sections. *Astrophys. J.* **896**, 148 (2020).

81. Massie, S. T. & Hunten, D. M. Stratospheric eddy diffusion coefficients from tracer data. *J. Geophys. Res. Atmos.* **86**, 9859–9868 (1981).

Acknowledgements

We thank M. Kirven-Brooks and C. P. McKay for support during the initial experimental phase at the NASA Ames Research Center. We are grateful to K. Weiss, S. Phrasavath, E. Soignard and A. Smith for help with the mineral analytics. We also thank J. G. Lopez for discussions on the diffusion modelling and A. D. Anbar, C. M. Ostrander, J. B. Glass, A. Kappler, M. J. Russell and S. Yoon for feedback on the manuscript. H.C.-Q. and S.B. were supported by the National Aeronautics and Space Administration's (NASA's) Nexus for Exoplanet System Science (NExSS) research coordination network at Arizona State University led by S. J. Desch (NNX-15AD53G) and sponsored by NASA's Science Mission Directorate. S.B. and H.I. received critical funding through the NASA Astrobiology Institute (NAI) Early Career Collaboration Award. H.I. also received funding for this work from the NASA Exoplanets Research Program and NExSS grant NNX-15AQ73G. The research was carried out in part at the Jet Propulsion Laboratory, California Institute of Technology, under a contract with NASA (80NM0018D0004). R.H. was supported in part by NASA's Exoplanets Research Program grant 80NM0018F0612. S.J.R. acknowledges support from NASA Exobiology (award 80NSSC19K0474) and the National Science Foundation Sedimentary Geology and Paleobiology Program (award 1733598).

Author contributions

S.B., H.I. and H.C.-Q. developed overall study objectives and the experimental design. S.B. performed the experiments. S.B., T.E. and S.J.R. conducted the thermodynamics and diffusion modelling. R.H. created the photochemical model. S.B. and H.C.-Q. drafted the manuscript. All authors participated in final revisions of the paper.

Competing interests

The authors declare no competing interests.

Additional information

Supplementary information The online version contains supplementary material available at https://doi.org/10.1038/s41561-022-01089-9.

Correspondence and requests for materials should be addressed to Steffen Buessecker.

Peer review information *Nature Geoscience* thanks Manabu Nishizawa, Sarah Rugheimer and the other, anonymous, reviewer(s) for their contribution to the peer review of this work. Primary Handling Editor: Rebecca Neely, in collaboration with the *Nature Geoscience* team.